Effect of thermal cycling and phase transformations on chemical life of ferritic stainless steels

Corrosion Science 264 (2026) 113779

Contents lists available at ScienceDirect

Corrosion Science

journal homepage: www.elsevier.com/locate/corsci

Effect of thermal cycling and phase transformations on chemical life of ferritic stainless steels

A. Chyrkin [a,*], D. Naumenko [b], M. Ziegner [b], E. Wessel [b], M. Sattari [c], J. Froitzheim [a]

[a] Chalmers University of Technology, Department of Chemistry and Chemical Engineering, Kemivägen 10, Gothenburg 412 96, Sweden
[b] Forschungszentrum Jülich GmbH, Institute of Energy Materials and Devices, IMD-1: Structure and Function of Materials, Wilhelm-Johnen-Straße, Jülich 52425, Germany
[c] Chalmers University of Technology, Department of Physics, Kemigården 1, Gothenburg 412 96, Sweden

ARTICLE INFO

Keywords:
Ferritic Stainless Steels
Oxidation
Breakaway Oxidation
Ferrite
Austenite
HT XRD

ABSTRACT

Thin foils (0.3 mm thick) of ferritic stainless steels Crofer 22 APU and Crofer 22 H typically used for SOFC/SOEC applications were isothermally and discontinuously oxidized in air for up to 1000 h at 1000 °C. Both steel grades suffered from breakaway oxidation, Crofer 22 APU failing faster (70 h) than Crofer 22 H (700 h). Counterintuitively, isothermal exposure of Crofer 22 APU resulted in a more severe corrosion attack compared to discontinuous exposures with intermediate cooling steps. In contrast, Crofer 22 H was not affected by the thermal history of exposure. Breakaway oxidation of both steel grades is related to the α-to-γ transformation occurring above 900 °C. Crofer 22 H is less susceptible to austenitization.

1. Introduction

Ferritic stainless steels based on the Fe-Cr system [1] find numerous industrial applications as structural materials in automotive exhaust systems [2], heat processing, power-plant boilers [3], etc. High-alloy ferritic steels have recently gained much attention as interconnect materials for solid oxide fuel cells (SOFCs) and electrolyzers (SOEC) [4–6].

The oxidation resistance of FeCr-based ferritic steels relies on the formation of slowly growing, well-adherent and protective Cr_2O_3 scales. Growth of Cr_2O_3 on the surface depletes the underlying metal of Cr, which is especially critical for thin-walled components such as thin sheets, foils, wires, porous metal foams, etc. Such products therefore have a limited chemical lifetime in service due to a critical depletion of Cr followed by breakaway oxidation, i.e., extremely rapid growth of Fe-rich oxides [7]. The time to breakaway or chemical lifetime can be accurately predicted as a function of the intrinsic properties of the alloys such as Cr reservoir (initial Cr concentration and component thickness) as well as environmental factors such as temperature affecting transport properties, oxide growth rate and Cr interdiffusion coefficient in the alloy. The available lifetime prediction tools, e.g., the mass-balance model by Quadakkers et al. [7,8] and the universal depletion model by Whittle [9,10] were recently reviewed in [11].

In our previous publication [11], we demonstrated that the α-to-γ phase-transformation occurring in the sharp corners/edges of the specimens is the key trigger of chemical failure for ferritic steels Crofer 22 APU and Crofer 22 H at and above 900 °C. Oxidation-induced austenitization of ferritic chromia-forming alloys has been hypothesized since the 1970s [12–14] and was recently confirmed by Chyrkin et al. for FeCr-based model alloys [15,16] via alloying them with ferrite-stabilizing (Mo) or austenite-stabilizing (Ni) elements. Austenitization of Crofer 22 APU and even Crofer 22 H was circumstantially demonstrated in the post-exposure microstructure of the respective steel samples [11] albeit after the transformation of γ back to α on cooling to room temperature. The austenitization affected zone (AAZ) was primarily found at the edges of the 0.3 mm thick foil specimens. At 1000 and 1050 °C, Crofer 22 APU formed a continuous layer of AAZ which gradually consumed the initial ferritic microstructure.

An unexpected reproducibility problem was revealed when exposures of Crofer 22 APU at 1000 °C were repeated isothermally (without intermediate cooling), compared with the standard discontinuous exposure (cooling every 24 or 48 h for weighing the specimens). The isothermal exposures resulted in a significantly more severe corrosion, i.e., entire oxidation of the foil specimen after 500 h, while the discontinuous specimens corroded only at the specimen edges up to 1000 h. At the same time, no such difficulties were encountered in reproducing the oxidation kinetics curve for Crofer 22 H irrespective of the exposure

* Corresponding author.
E-mail address: chyrkin@chalmers.se (A. Chyrkin).

https://doi.org/10.1016/j.corsci.2026.113779
Received 15 December 2025; Received in revised form 3 March 2026; Accepted 10 March 2026
Available online 11 March 2026

Table 1
Chemical composition in wt% of Crofer 22 APU and Crofer 22 H used in the present study.

	Fe	Cr	Mn	Si	Ti	W	Nb	C	La
Crofer 22 APU									
foil	Bal.	22.9	0.38	0.01	0.06	-	-	0.004	0.09
powder	Bal.	22.3	0.43	0.03	0.047	-	-	0.009	0.001
Crofer 22 H									
foil	Bal.	22.6	0.43	0.24	0.06	1.97	0.49	0.009	0.05

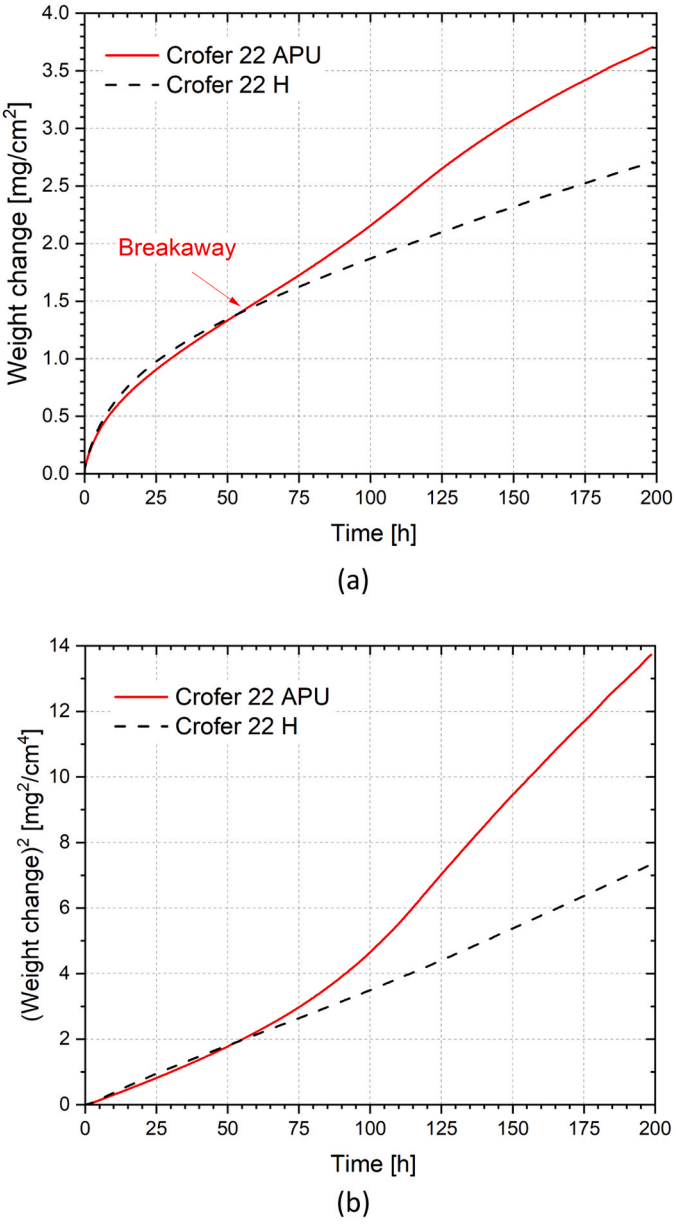

Fig. 1. In-situ recorded weight change for 0.3 mm thick foils of Crofer 22 APU (red solid line) and Crofer 22 H (black dashed line) exposed isothermally for 200 h to synthetic air at 1000 °C in thermobalance.

mode: isothermal or discontinuous. Experiments with another batch of Crofer 22 APU resulted in the same oxidation pattern, i.e., thermal cycling appeared, counterintuitively, beneficial for the oxidation resistance of the steel.

The goal of the present study is thus to systematically explore the effect of thermal cycling on oxidation resistance and lifetime of 0.3 mm thick foils of Crofer 22 APU and Crofer 22 H at 1000 °C in air and

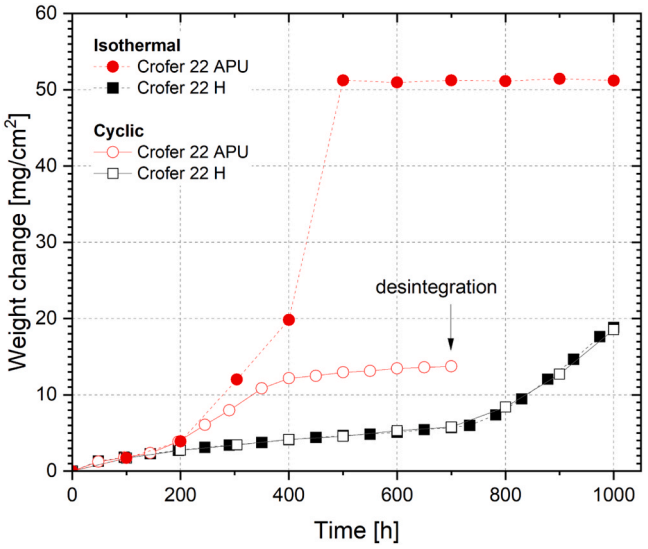

Fig. 2. Weight change for Crofer 22 APU (circles) and Crofer 22 H (squares) foils during cyclic (empty symbols) and isothermal (full symbols) air oxidation for up to 1000 h at 1000 °C.

Table 2
Weight change of 0.3 mm thick foils of Crofer 22 APU and Crofer 22 H after 200 h of isothermal air exposure at 1000 °C in tubular furnace and thermobalance.

Experiment	Weight change [mg cm^{-2}]	
	Crofer 22 APU	Crofer 22 H
Furnace exposure	3.87	2.73
Thermobalance	3.75	2.74

elucidate the underlying mechanism behind the effect of thermal history on the lifetime of ferritic steels such as Crofer 22 APU and Crofer 22 H. To that end, the specimens were exposed in two different modes: i) isothermal – one exposure is one data point and ii) discontinuous – the specimens were cooled and re-heated every 48 h. The microstructural and compositional evolution in the foils was investigated by scanning electron microscopy (SEM) with energy dispersive X-ray spectroscopy (EDX), electron backscatter diffraction (EBSD) and transmission electron microscopy (TEM) along with EDX and electron diffraction. Additionally, the α-to-γ transformation was studied in-situ via high-temperature X-ray diffraction (HT XRD) of Crofer 22 APU powder.

2. Experimental

2.1. Materials

The 0.3 mm thick sheets of Crofer 22 APU and Crofer 22 H in bright annealed state were supplied by VDM Metals (Werdohl, Germany). The powder of Crofer 22 APU was supplied by Rosswag GmbH (Pfinztal, Germany). The particle size varied from approximately 15–45 μm. The chemical compositions of all materials used in the present study are

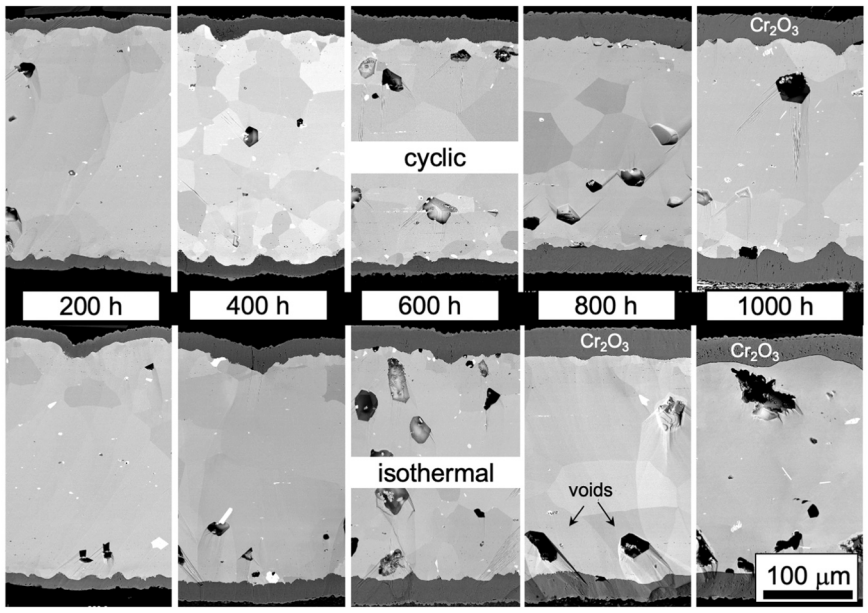

(a)

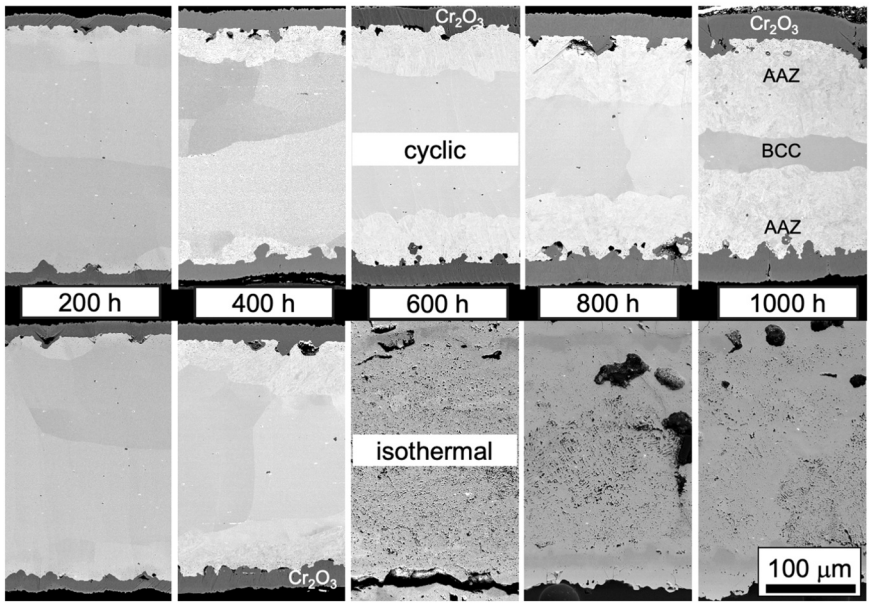

(b)

Fig. 3. BSE images of cross-sectioned foils of (a) Crofer 22 H and (b) Crofer 22 APU after cyclic and isothermal oxidation for up to 1000 h in lab air at 1000 °C.

listed in Table 1. Rectangular test coupons measuring 15 × 15 mm^2 were cut from the sheets and degreased with acetone and ethanol prior to exposure.

2.2. Thermobalance exposures

The *in-situ* oxidation kinetics measurements were isothermally performed with a SETARAM thermobalance in flowing synthetic air for up to 200 h at 1000 °C. The heating rate was 90 K min^{-1}. The cooling rate was 10 K min^{-1}.

2.3. Furnace exposures

Exposures of the steel samples were carried out in a horizontal tubular furnace with an inner diameter of 46 mm. Each test coupon was suspended via a 2 mm hole drilled into the coupon, mounted on a 1 mm thick alumina rod, and placed within a boat-shaped alumina crucible. All exposures were carried out in stagnant lab air. For each exposure, three steel coupons were tested to ensure reproducibility. The specimen holder was immediately introduced into the hot zone of the furnace and rapidly moved into the cold zone of the furnace after the dwell time. Mass gains were measured at every cooling step with a Mettler Toledo microbalance.

Two types of oxidation exposures were undertaken. The discontinuous exposures were interrupted every 48 h for weighing the specimens. For the sake of simplicity, these exposures will be referred to as the cyclic ones. Isothermal exposures were performed without interruption. Every isothermal weight gain data point corresponds to an individual

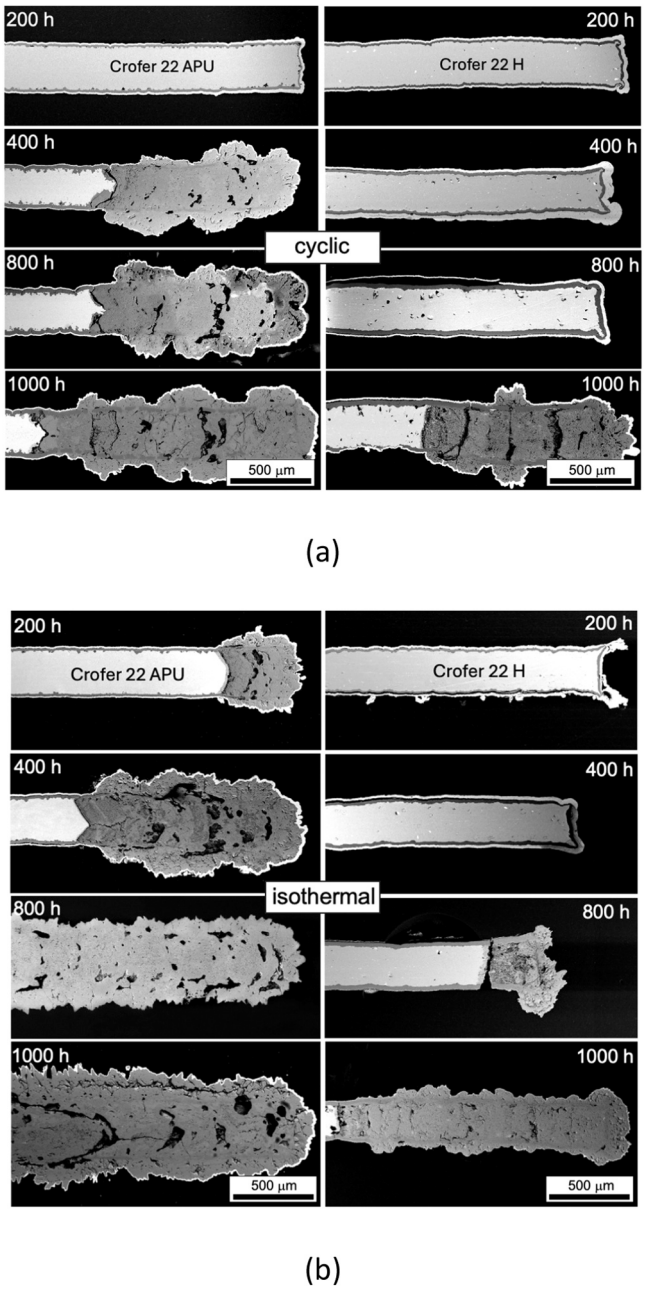

Fig. 4. BSE images of cross-sectioned foils of Crofer 22 APU (left column) and Crofer 22 H (right column) demonstrating temporal evolution of specimen edges during (a) cyclic and (b) isothermal oxidation in air for up to 1000 h at 1000 °C.

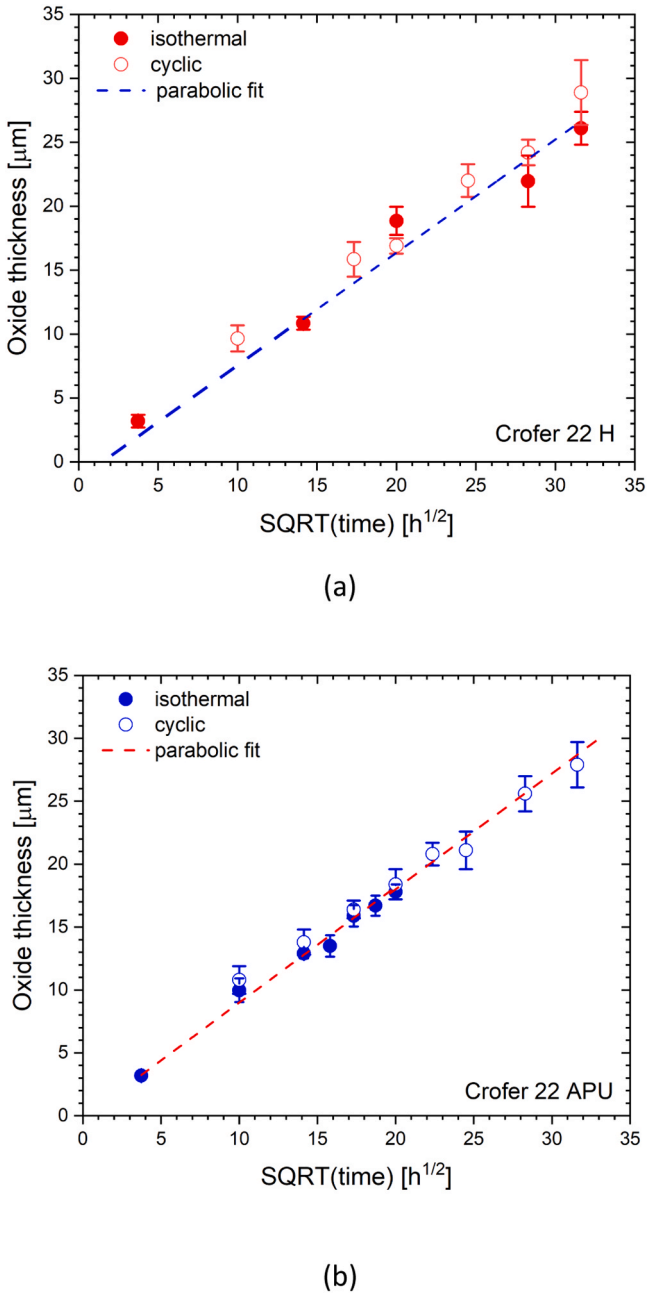

Fig. 5. Oxide scaling kinetics determined from BSE images for (a) Crofer 22 H and (b) Crofer 22 APU foils after isothermal (full symbols) and cyclic (empty symbols) air oxidation for up to 1000 h at 1000 °C.

exposure, the specimens being weighed before and after the exposure.

2.4. Scanning electron microscopy, SEM

Cross-sections of the exposed steel specimens were prepared using a Leica TIC 3X broad ion beam (BIB) for SEM-EDX analysis. An FEI ESEM QUANTA 200 equipped with an Oxford X-max 80 EDX detector was used for cross-sectional SEM-EDX analyses of the BIB cross-sections. The SEM was operated at an accelerating voltage of 10–20 kV in high vacuum. The working distance was 10 mm.

Selected specimens were cold mounted in epoxy resin to metallographically prepare full-length cross-sections and investigate the corroded edges of the foils. The latter specimens were gold-sputtered and electroplated with Ni prior to mounting. The mounted specimens were mechanically ground to 4000 grit and polished with diamond pastes to 0.25 µm surface finish.

2.5. Electron backscatter diffraction, EBSD

Electron backscatter diffraction (EBSD) phase contrast maps as well as Kernel misorientation maps (KAM) were obtained using a FIB-SIM TESCAN GAIA 3. The microscope was operated at 20 kV with a collection speed of 637.76 Hz and scanning step of 0.1 µm. The local misorientation was analyzed in a 3 × 3 matrix with a maximum angle of 2°.

2.6. Focused ion beam/scanning electron microscopy, FIB/SEM

An FEI Versa 3D combined Focused Ion Beam/SEM (FIB/SEM) workstation was used to produce cross-section thin foils from the oxide

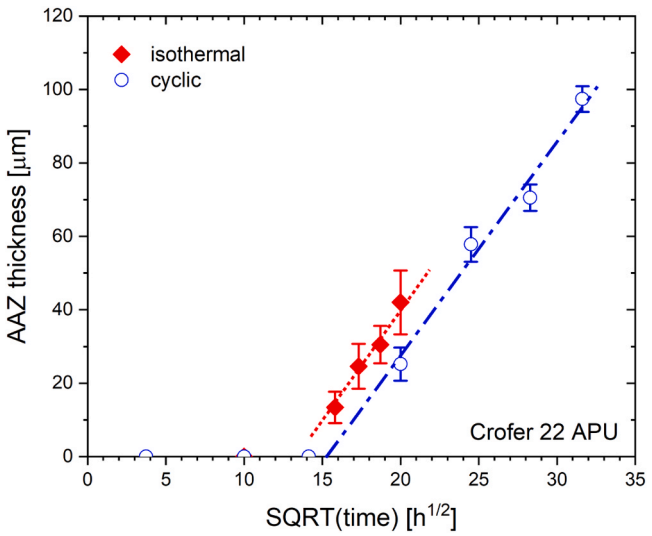

Fig. 6. Kinetics of thickening of the austenitization affected zone (AAZ) in Crofer 22 APU determined from BSE images after isothermal and cyclic air oxidation for up to 1000 h at 1000 °C.

scale and subjacent metal. To protect the TEM specimen during the subsequent ion milling, a thin Pt layer was first deposited with the aid of electrons on the surface (25 × 5 μm^2) and then a thicker Pt layer (with a thickness of ~2 μm) was deposited on top using Ga-ions. At the initial stages of the milling, higher ion currents were used, while lower currents were chosen at the final stages to produce finer surfaces. Lower ion energies (2 and 5 kV with ion currents of 49 and 27 nA, respectively) were selected in the final stages of polishing to minimize the potential artefacts from FIB milling.

2.7. Scanning transmission electron microscopy, STEM

Scanning transmission electron microscopy (STEM) was performed using a JEOL ARM 200 F TEM/STEM equipped with an Oxford Instruments EDS detector and a FEG to acquire STEM micrographs in High Angle Annular Dark Field (HAADF) and Bright Field (BF) modes as well as to obtain electron diffraction patterns. Selected area electron diffraction (SAED) patterns were processed in the CrysTBox software [17].

2.8. Transmission kikuchi diffraction, TKD

Transmission Kikuchi diffraction (TKD) maps were acquired using a LEO Ultra 55 FEG-SEM equipped with an HKL Channel 5 EBSD system with a Nordlys II detector on thin-foil specimens extracted by the FIB/SEM technique for STEM analyses. The analyses were performed using parameters described in [18].

2.9. High-temperature X-ray diffraction

An Empyrean diffractometer (Malvern Panalytical) equipped with a Cu-LFF X-ray tube (operated at 40 kV and 40 mA), Bragg-Brentano HD mirror with 0.4° divergence, a PIXcel3D detector in 1D mode and a high temperature oven chamber Anton Paar HTK 1200 N was used for the in-situ powder diffraction experiments. The Crofer 22 APU powder samples were heated in air with 90 K/min to the target temperature of 900 °C or 1000 °C and subsequently diffractograms were recorded. Due to fast transformation, especially at 1000 °C, a short measurement time per scan was necessary. A 2θ range of 32°–45° which contains the strongest Bragg reflections of all observed phases, a step size of 0.0525° and a step time of 0.2 s were chosen. This results in an overall measurement time of 1.3 min.

Diffraction data were analyzed by the Rietveld method using the TOPAS software (version 6, Bruker AXS) and crystal structures retrieved from the Inorganic Crystal Structure Database (ICSD).

3. Results

3.1. Isothermal vs cyclic oxidation

Fig. 1 shows *in-situ* recorded oxygen uptakes by 0.3 mm thick foils of Crofer 22 APU and Crofer 22 H isothermally exposed in synthetic air for 200 h at 1000 °C. Initially, both steel grades obey a parabolic time law for oxidation and reveal a nearly identical parabolic rate constant for up to 50 h of exposure. After approximately 70 h, the weight change for Crofer 22 APU accelerates (Fig. 1**a**) while the oxidation kinetics of Crofer 22 H remains protective and parabolic for at least 200 h (Fig. 1**b**).

Fig. 2 compares oxygen uptake by foil specimens of Crofer 22 APU and Crofer 22 H during isothermal and cyclic furnace exposures in lab air at 1000 °C for up to 1000 h. Irrespective of the exposure mode, both steel grades suffered from breakaway oxidation: Crofer 22 APU after 100 h and Crofer 22 H after 700 h, respectively. The weight change values obtained in the discontinuous furnace exposures were in very good agreement with the in-situ TG-experiments (Fig. 1) as demonstrated in Table 2 for the specimens isothermally exposed in air for 200 h at 1000 °C.

The exposure mode had no effect on Crofer 22 H, i.e., the isothermal weight gain curve coincides with the cyclic one in both protective and breakaway regimes. For Crofer 22 APU, the situation is different. In the protective regime (up to 100 h), the isothermal and cyclic Crofer 22 APU specimens demonstrated the same oxygen uptake. After the onset of breakaway, the isothermal specimens revealed a faster oxidation rate

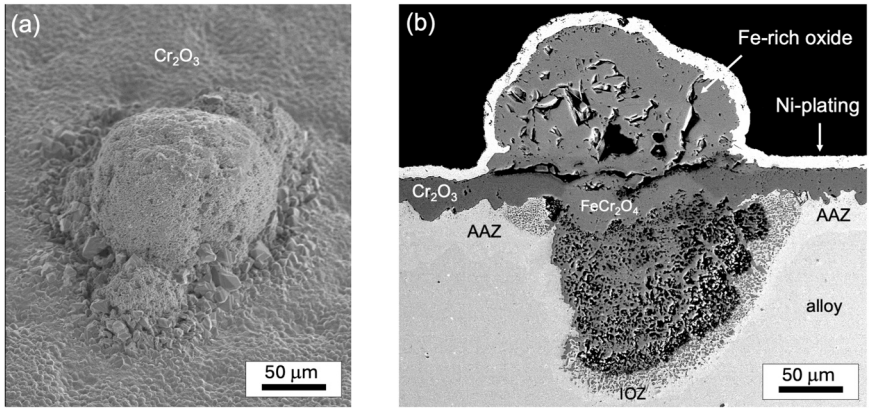

Fig. 7. Oxide nodule formed on Crofer 22 APU foil after 400 h isothermal air oxidation at 1000 °C: (a) SE top-view image and (b) BSE image of cross-sectioned foil.

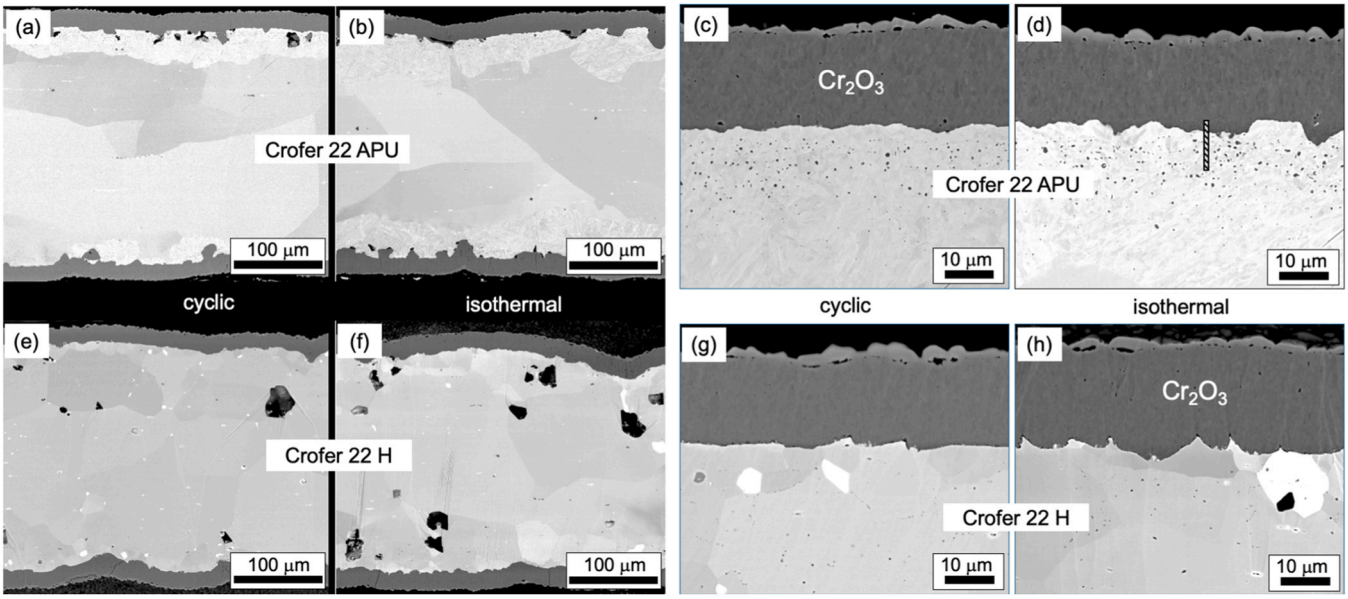

Fig. 8. BSE images comparing foils of Crofer 22 APU (a-d) and Crofer 22 H (e-h) after 400 h cyclic and isothermal air oxidation at 1000 °C: overview (a,b,e,f) and oxide scales (c,d,g,h). The bar in the upper right micrograph schematically shows sampling for TEM analysis.

compared to the cyclic ones and reached a weight gain plateau after 500 h. The average oxygen uptake of 51.5 mg/cm^2 of the foil specimens corresponds to a stoichiometric ratio $MO_{0.33}$ or M_3O_4 (M = Fe and/or Cr) and implies a complete through-thickness oxidation of the Crofer 22 APU foils after 500 h of isothermal oxidation at 1000 °C. The cycled Crofer 22 APU specimens demonstrated accelerated oxidation as well. However, the oxidation rate significantly decreased after 400 h, the slope of the oxidation curve being close to that of Crofer 22 H after 700 h.

BSE SEM images in Fig. 3 illustrate temporal evolution of the Crofer 22 H and Crofer 22 APU specimens during isothermal and cyclic air oxidation for up to 1000 h at 1000 °C. Oxidation of the Crofer 22 H foils is featured by i) gradual thickening of the Cr_2O_3 scales on the surface, ii) slow coarsening of the alloy grains, and iii) formation of cavities. No significant differences could be established between the isothermal and cyclic exposures of Crofer 22 H, in agreement with the weight change curve in Fig. 2.

The oxidation behavior of Crofer 22 APU is more complicated. In contrast to Crofer 22 H, the grade Crofer 22 APU upon oxidation at 1000 °C reveals i) rapid grain coarsening, ii) no cavities, iii) formation of a new bright-contrast layer termed as austenitization affected zone (AAZ) underneath the Cr_2O_3 scale, and iv) complete catastrophic oxidation of the foils after 400 h if exposed isothermally. Surprisingly, Crofer 22 APU demonstrates a better oxidation resistance during thermal cycling.

BSE SEM images in Fig. 4 demonstrate the temporal microstructural evolution of the foil edges of Crofer 22 APU and Crofer 22 H during isothermal and cyclic air oxidation at 1000 °C. It is important to stress that breakaway corrosion shown in Fig. 4 was exclusively limited to the edges of the foils. In the cyclic exposures (Fig. 4**a**), breakaway corrosion at the edges of the Crofer 22 APU foil appeared after 400 h and further laterally progressed into the specimen. Crofer 22 H demonstrated a protective behavior of the foil edges for up to 800 h, but eventually developed a similar corrosion pattern as Crofer 22 APU at earlier stages. The isothermal exposures (Fig. 4**b**) revealed two significant differences from the cyclic experiments. First, both Crofer 22 APU and Crofer 22 H showed earlier signs of breakaway oxidation at the edges during isothermal exposures. Second, Crofer 22 APU suffered from total through-thickness oxidation (see also Fig. 3**b**).

Fig. 5 displays Cr_2O_3 thickness as a function of time in the sound areas where the Cr_2O_3 scale remained protective plotted as a function of $\sqrt{t}$. The scaling kinetics of both steel grades obeys the parabolic time-law. No significant differences could be established between the cyclic and isothermal specimens of both steels. In other words, the mode of exposure had no effect on the oxidation rate. The parabolic rate constants calculated in terms of metal recession, k_c, were 2.7×10^{-17} m^{2}s^{-1} for Crofer 22 APU and 2.5×10^{-17} m^{2}s^{-1} for Crofer 22 H, respectively, in very good agreement with our previous work [11].

Fig. 6 displays the thickening kinetics of the AAZ in the Crofer 22 APU foils during isothermal and cyclic air oxidation for up to 1000 h at 1000 °C. The AAZ thickness was measured in the corresponding SEM images. The AAZ (Fig. 3**b**) appears after a certain incubation time. Extrapolation of the more populated cyclic data to zero thickness yields 225 h. According to the microscopic observations, the AAZ layer forms between 200 and 300 h. The growth kinetics of the AAZ layer is parabolic, i.e., diffusion controlled. The parabolic rate constant determined from the slope of the linear fit in Fig. 6 is 1.3×10^{-15} m^{2}s^{-1}, which is close to the interdiffusion coefficient of Cr in FCC at 1000 °C, 1.5×10^{-15} m^{2}s^{-1} [19]. In the isothermal exposures, the AAZ seems to appear earlier, however, the slope and thus the growth rate does not differ from the cyclic data. The latter conclusion should be made with utmost care as the number of data points in the isothermal experiment is limited due to catastrophic oxidation occurring in the isothermal Crofer 22 APU specimens after 400 h.

3.2. *Crofer 22 APU after 400 h – critical point*

The catastrophic, through-thickness oxidation of the Crofer 22 APU foils during isothermal oxidation was an unexpected result considering the fact that the cyclic samples remained protective in the middle of the foils up to 1000 h of exposure. The opposite behavior is generally reported in most oxidation studies, i.e., thermal cycling is a detrimental factor accelerating corrosion effects and degradation. The experimental campaigns were repeated three times to ensure reproducibility of this effect. It is obvious that a critical change occurred in the isothermally oxidized Crofer 22 APU foils between 400 and 500 h that gave rise to a catastrophic oxidation, not occurring in the cyclic exposures. In this section, we will put more focus on the specimens after 400 h, i.e., the last data point prior to catastrophic oxidation of the isothermal specimens.

A notable difference between the isothermal and cycled foils of Crofer 22 APU were protruding oxide nodules on the surface of the

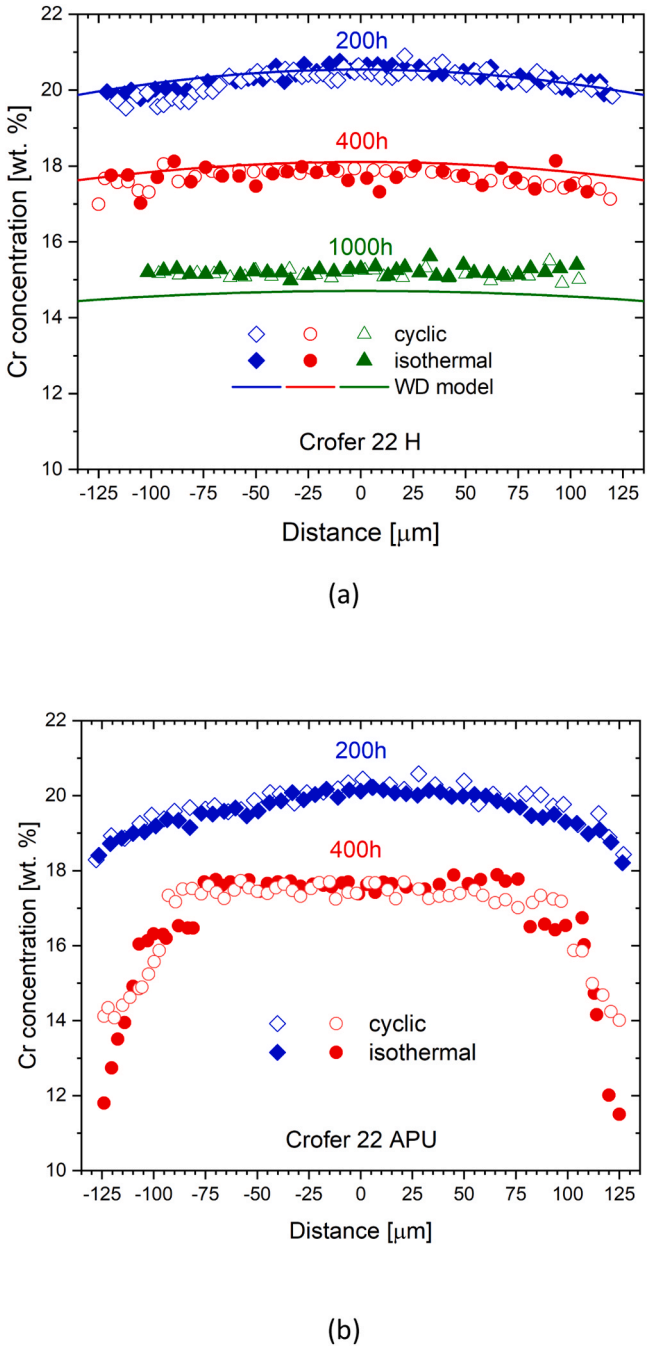

Fig. 9. Cr-concentration profiles in (a) Crofer 22 H and (b)Crofer 22 APU foils after isothermal (full symbols) and cyclic (empty symbols) air oxidation at 1000 °C. Cr concentrations were measured with EDX in cross-sectioned specimens after 200, 400, 1000 h.

isothermal specimen. Fig. 7**a** shows a top-view SE image of a characteristic oxide nodule grown on the surface of Crofer 22 APU after 400 h of isothermal oxidation at 1000 °C. The nodule is approximately 100 μm in diameter. Fig. 7**b** shows a BSE SEM image of a similar nodule grown on the same specimen in cross-section. The outer part of the nodule is Fe-rich oxide. The oxide layer underneath the nodule has a brighter contrast, which is indicative of the transformation of Cr_2O_3 into $FeCr_2O_4$. The spinel layer is followed by a porous mass of internal (Fe, Cr)-rich oxide (EDX analysis not shown here). Finally, the innermost layer is a classical internal oxidation zone (IOZ) containing dispersed (Fe,Cr)-rich oxides. A layer of AAZ is visible underneath the sound Cr_2O_3 as well as along the IOZ in the inner part of the breakaway nodule. The

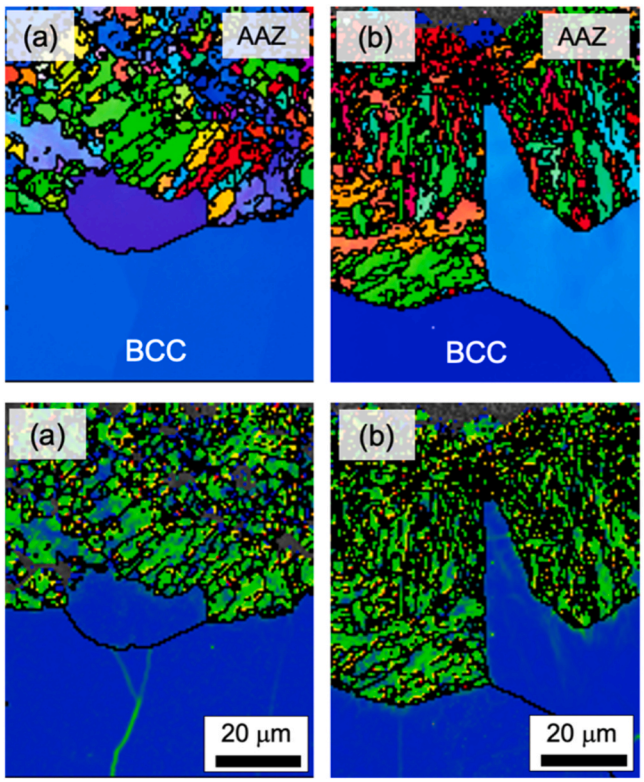

Fig. 10. EBSD (a,b) and Kernel misorientation map (KAM) of BCC phase in Crofer 22 APU foil specimen after 400 h of isothermal (a,c) and cyclic (b,d) exposure in air at 1000 °C. AAZ denotes austenitization affected zone.

IOZs in the immediate vicinity of the outer Cr_2O_3 on both sides of the nodule suggest a critical depletion of Cr and transition from external to internal oxidation. Clearly, internal/breakaway oxidation and propagation of AAZ are closely related.

It is suggested that the spherical nodules are triggered by defects that act as local weak points such as precipitate inclusions on the surface triggering the nodule formation. Such a precipitate particle creates a sharp edge in the plane surface and thus promotes an enhanced local depletion of Cr, austenitization and the ensuing local Cr depletion to virtually zero while the area around the nodule is still covered with protective Cr_2O_3. Once the spot is critically depleted of Cr, three parallel phenomena start to locally govern the oxidation process: i) Cr oxidizes internally in the underlying Cr-depleted alloy and forms internal $(Fe, Cr)_3O_4$ precipitates [14], ii) Fe oxidizes externally forming the outer nodule, iii) the Cr-free metal between the precipitates in the IOZ (mainly pure iron) oxidizes inwards. Further lateral spreading of these nodules eventually leads to the complete through-thickness oxidation of the isothermally exposed Crofer 22 APU foils.

Fig. 8 displays BSE SEM images taken in the middle of cross-sectioned Crofer 22 APU and Crofer 22 H foils after 400 h of isothermal and cyclic air exposures at 1000 °C. Two main observations can be made based on these BSE images: i) thermal cycling does not affect oxide thickness (in agreement with Fig. 5), ii) the AAZ in Crofer 22 APU is thicker in the isothermal specimen compared to the cycled one (in agreement with Fig. 6).

To better understand transport phenomena in the studied foil specimens, Cr-concentration profiles presented in Fig. 9 were measured across the foil thickness for Crofer 22 H and Crofer 22 APU after isothermal and cyclic air exposures at 1000 °C. The Cr-profiles in Crofer 22 H (Fig. 9**a**) have a classical rainbow-shaped form of depletion profiles and can be well approximated with the Whittle depletion (WD) model [9,10] as described e.g. in [11]. The interdiffusion coefficient of, $\widetilde{D}_{Cr}$, for ferritic BCC lattice, 3.6×10^{-14} m^2s^{-1}, was taken from [19] while the

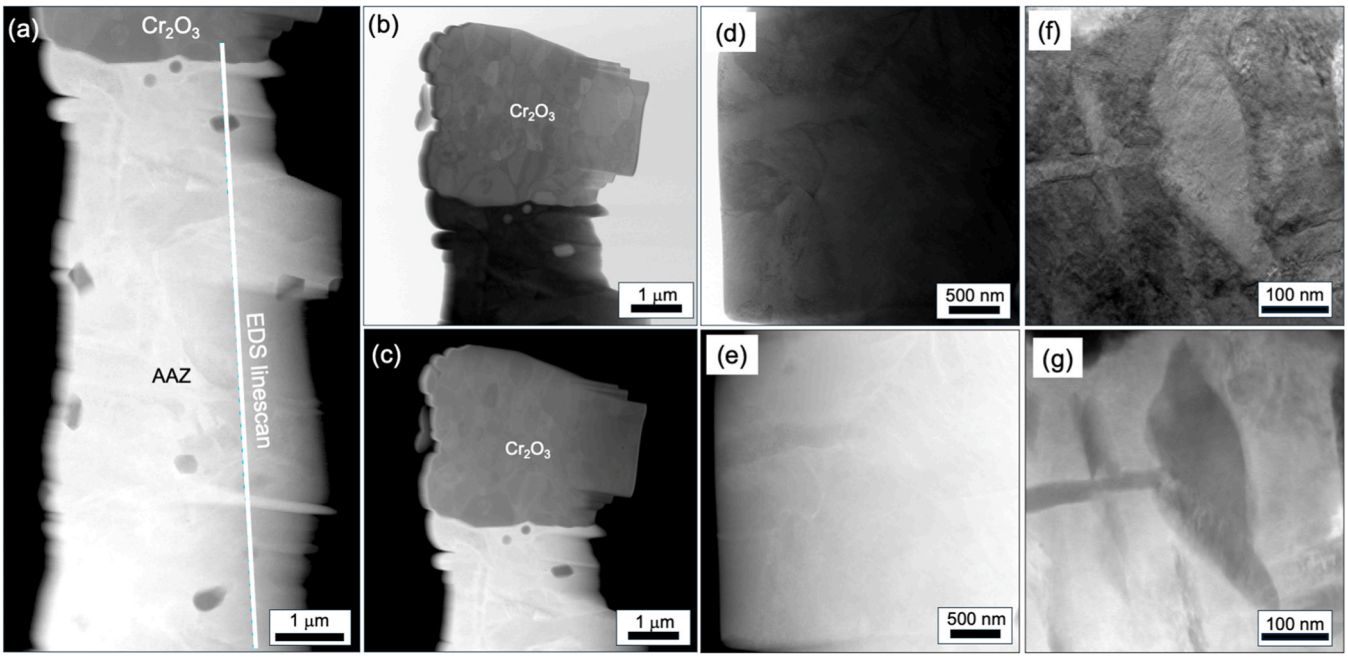

Fig. 11. HAADF (a,c,e,g) and BF (b,d,f) TEM images of AAZ in Crofer 22 APU foil after 400 h of isothermal air oxidation at 1000 °C in the immediate vicinity of the oxide-alloy interface. White line in Fig. (a) marks the EDX linescan position.

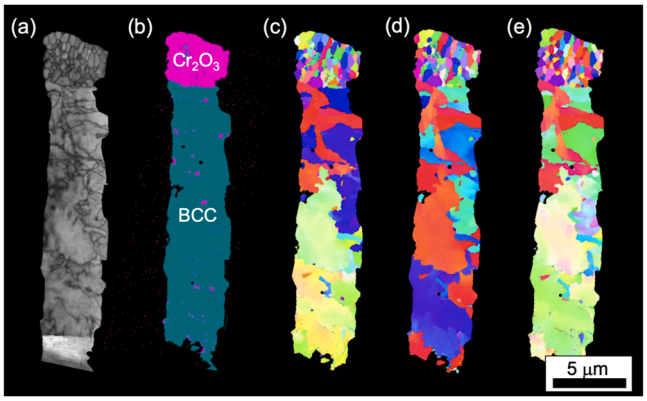

Fig. 12. TKD orientation maps of AAZ in the Crofer 22 APU foil after 400 h of isothermal air oxidation at 1000 °C: a) band contrast, b) phase contrast, c) IPF-X, d) IPF-Y, e) IPF-Z.

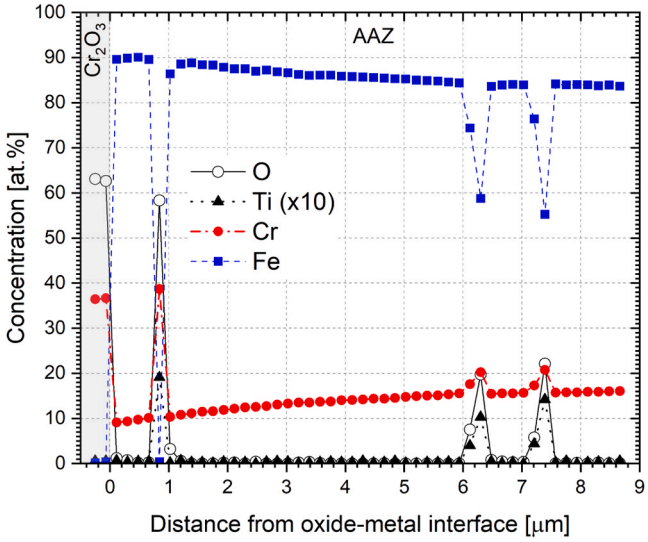

Fig. 13. Concentration profiles of Fe, Cr, Ti and O measured in AAZ of the Crofer 22 APU foil after 400 h of isothermal air oxidation at 1000 °C. Measured with EDX in the TEM lamella as shown in Fig. 11.

oxidation rate, k_c, for Crofer 22 H was adopted from our own experiment (Fig. 5). The WD model accurately predicted the Cr-depletion dynamics in the Crofer 22 H foils. More importantly, thermal cycling had no measurable effect on Cr depletion, i.e., the measured Cr-profiles in the isothermal specimens match those measured in the cycled specimens.

The situation is different in Crofer 22 APU (Fig. 9**b**). The Cr-depletion profiles were measured only after 200 and 400 h because of complete oxidation of the isothermal Crofer 22 APU specimens after 400 h. Initially, the Cr-depletion pattern of Crofer 22 APU is very similar to that of Crofer 22 H, i.e., almost identical rainbow-shaped curves were measured in Crofer 22 APU after 200 h on both isothermal and cycled specimens. After 400 h, the Cr-profiles in Crofer 22 APU are not continuous. In the immediate vicinity of the oxide-metal interface the Cr-concentration profile is steep indicating a slower diffusion of Cr compared to the original ferritic alloy matrix. The steep sections of the Cr-profiles correlate with the AAZ observed in BSE images (Fig. 8). Most interestingly, the Cr-profiles in the isothermal Crofer 22 APU specimen are steeper (11 wt% Cr at the oxide-metal interface) than the Cr-profiles in the cycled specimen (14 wt% Cr at the oxide-metal interface). The latter implies a faster Cr diffusion through the FCC layer (observed as AAZ in the BSE cross-sections) during the exposure.

3.3. *Microstructure of AAZ*

EBSD phase contrast and KAM (Kernel misorientation) maps in Fig. 10 show that the AAZ formed in the Crofer 22 APU specimen is fine-grained ferrite (BCC). No significant differences could be found in the AAZ formed in the isothermal and the cycled specimen: neither in the grain size nor in the misorientation degree distribution. Apparently, one cooling is enough to produce a fine-grain microstructure in the AAZ and secure thus fast-track grain-boundary diffusion through this layer.

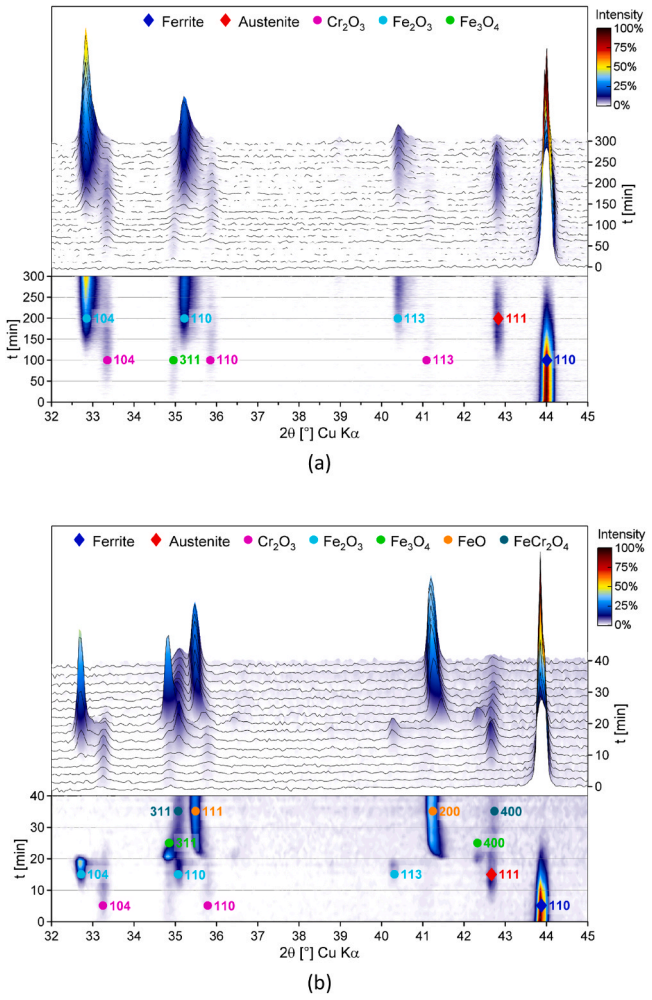

Fig. 14. High-temperature in-situ XRD analysis of Crofer 22 APU powder during heating in air at (a) 900 °C and (b) 1000 °C. Colored markers at the positions of characteristic Bragg reflections: blue – ferrite (110), red – austenite (111), magenta – Cr_2O_3 (104, 110), cyan - Fe_2O_3 (104, 110, 113), green – Fe_3O_4 (311, 400), dark cyan – $FeCr_2O_4$ (311, 400), orange – FeO (111, 200).

TEM images displayed in Fig. 11 confirm the fine-grained microstructure of AAZ in the Crofer 22 APU foil isothermally exposed in air for 400 h at 1000 °C. The AAZ contains grains ranging in size from 0.2 to 1 μm in the intermediate vicinity of the oxide-alloy interface along with internal (Cr,Ti)-rich oxide particles. According to electron diffraction patterns (Fig. S7 in **Data supplement**), the small grains are ferritic (BCC). The BCC lattice in the entire AAZ was additionally confirmed by the TKD analysis (Fig. 12) of the TEM lamella shown in Fig. 11. An EDX line-scan measured across the AAZ towards the Cr_2O_3 oxide scale shown in Fig. 13 measures the Cr concentration at the oxide-metal interface to be close to 10 at% in agreement with the Cr concentration profiles in Fig. 9**b** measured with SEM EDX.

3.4. *In-situ X-ray diffraction*

The post-mortem analyses of the AAZs presented in Fig. 9- Fig. 12 provide strong indirect evidence to interpret the microstructural changes observed in Crofer 22 APU and thus the trigger of breakaway oxidation as the α-to-γ phase transformation. However, this evidence is still circumstantial. In-situ diffraction would be therefore a perfect experimental proof of the austenitization mechanism. An HT XRD experiment on thin alloy foils, as presented e.g. in Fig. 3 is, however, experimentally challenging for two reasons:

- FCC appears after 225 h (Fig. 6) which is too long for an in-situ HT XRD experiment without intermediate cooling steps or pre-oxidation.
- More importantly, the Cr_2O_3 scale is already 15 μm thick (Fig. 5) by the time the austenite starts to emerge, which makes it difficult to reasonably acquire the diffraction patterns from the underlying alloy.

To overcome both difficulties, Crofer 22 APU powder was used for HT XRD instead: i) the small powder particles, due to their large surface/volume ratio, are readily depleted of Cr to the critical austenitization threshold within tens of minutes and ii) the oxide scale remains thin and does not interfere with the measurement.

Fig. 14 presents XRD diffractograms measured on powder of Crofer 22 APU using in-situ high-temperature XRD at 900 (Fig. 14**a**) and 1000 °C (Fig. 14**b**). At room temperature (Fig. S1 in **Data supplement**), Crofer 22 APU is fully ferritic. The oxidation process at 900 and 1000 °C is featured initially by the Bragg reflections of Cr_2O_3 and Fe_3O_4 concluding the reaction with the formation of Fe_2O_3 in the later stages signaling breakaway oxidation. A characteristic peak of austenite (reflection 111 at 42.8 °) emerges after 60 min at 900 °C and 7 min at 1000 °C (see the detailed temporal evolution of the XRD patterns during high-temperature exposures, the cooling process and after oxidation in Figs S2-S6 in **Data supplement**). Clearly, the formation of austenite precedes breakaway oxidation. The austenite transformed back into ferrite on cooling (Figs S3 and S6 in **Data supplement**).

Fig. 15 shows the BSE SEM images of cross-sectioned specimens of Crofer 22 APU powders prior to and after exposures in the HT X-ray diffractometer. The as-received alloy powder contained particles of 15–45 μm in diameter in agreement with the powder specification. After high-temperature exposures at 900 and 1000 °C, smaller powder particles were completely oxidized while the bigger particles were covered with a thin layer of Cr_2O_3.

4. Discussion

4.1. *Austenitization*

4.1.1. *Crofer 22 APU*

Ferritic stainless steels such as Crofer 22 APU [4,20] and Crofer 22 H [21,22] are based on the binary Fe-Cr alloy system [23] in which the body-centered cubic (BCC) structure dominates. Similar to pure iron, at high temperature the Fe-Cr alloys may transform to austenite with a face-centered cubic (FCC) structure. The transition temperatures depend on the exact composition, the austenite or γ-loop extending between 846 and 1392 °C and from zero to 11.0 wt% in terms of Cr content. Fig. 16**a** displays a part of the Fe-Cr phase diagram calculated in Thermo-Calc using the TCFE9 database [24]. Given its chemical composition (Table 1), Crofer 22 APU can be reasonably approximated as Fe-Cr as discussed in [11]. At the beginning of the exposure at 1000 °C (point A), the alloy is ferritic. As oxidation of Crofer 22 APU proceeds, the growth of Cr_2O_3 on the surface depletes the alloy of Cr (Fig. 9) reaching after a certain time the α/γ-boundary (13.5 wt%, point B in Fig. 16**a**).

The γ-FCC phase forms at the most Cr-depleted site, i.e., in the immediate vicinity of the oxide-metal interface (Fig. 3**b**). The Cr depletion process is well-known to be more intense at the corners and edges of the specimens due to a higher surface-to-volume ratio [25], the alloy volume being depleted of Cr faster from multiple surfaces. Therefore, the afore-mentioned α-to-γ transformation is more likely to initiate earlier at the corners/edges (Fig. 4) than underneath a flat Cr_2O_3 scale growing on the alloy (Fig. 3**b**). The formation of FCC further depletes the oxide-metal interface of Cr as Cr diffusion in austenitic iron (FCC) is almost an order of magnitude slower compared to ferritic iron (BCC): at 1000 °C, $\widetilde{D}_{Cr}^{FCC} = 1.5 \times 10^{-15}$ while $\widetilde{D}_{Cr}^{BCC} = 3.6 \times 10^{-14}$ [19]. The slower Cr transport in FCC impedes the Cr supply to the oxide-metal interface

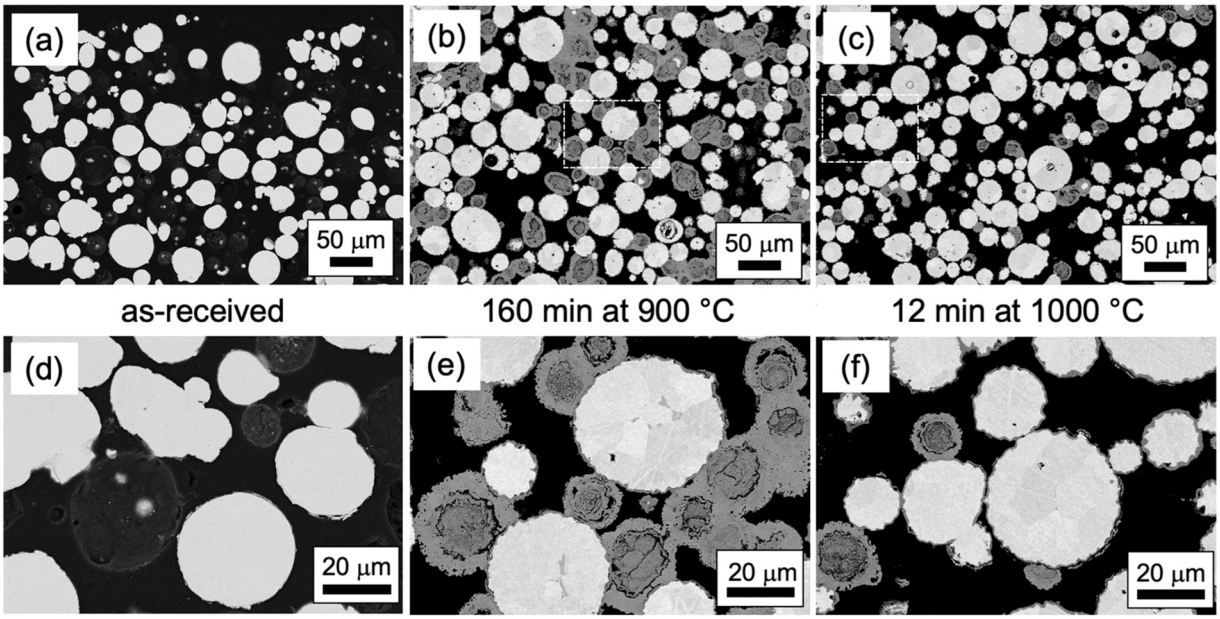

Fig. 15. BSE SEM micrographs of sectioned powder specimen of Crofer 22 APU before (a,d) and after air oxidation for (b,e) 160 min at 900 °C and (c,f) 12 min at 1000 °C. The frames in low-magnification images indicate the sampling area.

lowering the interfacial concentration of Cr. The enhanced Cr depletion at the oxide-metal interface is clearly observed in Crofer 22 APU after 400 h (Fig. 9**b** and Fig. 13). Oxidation-induced austenitization of Crofer 22 APU has been previously demonstrated to occur at 950–1050 °C by Chyrkin and Froitzheim [11]. These post-mortem morphologies were fully reproduced in the present study (Fig. 3**b**). At the same time, the entire evidence of austenitization in Crofer 22 APU presented in [11] was circumstantial and based on the analyses of the cooled specimens after the α-to-γ transformation had occurred. To experimentally validate the austenitization mechanism, an in-situ high-temperature X-ray diffraction experiment was undertaken on powder of Crofer 22 APU. Small powder particles (15–41 µm) were expected to be rapidly depleted of Cr to reach the austenitization threshold (13–15 wt% Cr) within hours (900 °C) or even minutes (1000 °C) and subsequently suffer from breakaway oxidation as can be seen in the post-exposure micrographs of the powders in Fig. 15. The HT diffractograms in Fig. 14 (see also Figs S2-S6 in **Data supplement**) unequivocally demonstrate the presence of austenite (FCC) in the Crofer 22 APU powder during the air exposures at 900 and 1000 °C. On cooling, the FCC phase transformed back to BCC (AAZ).

4.1.2. *Crofer 22 H*

Austenitization can occur in Crofer 22 H as well. The latter steel grade was developed based on the chemical composition of Crofer 22 APU (Table 1) via further alloying with W, Si and Nb to improve the alloy creep strength introducing the Laves-phase into the microstructure. Alloying with W had an additional solution strengthening effect while the Laves-phase had a high solubility for Si tying it up and decreasing its availability for internal oxidation [21,22]. All three alloying additions are well-known ferrite stabilizers [26]. Fig. 16**b** shows the calculated γ-loop for Crofer 22 H using the TCFE9 database [24] as well as the alloy composition from Table 1. The construction of the phase diagram for Crofer 22 H is described in detail in [11]. Alloying with W, Nb and Si resulted in a shrinkage of the γ-loop. At 1000 °C, the α/γ-boundary (point B) is shifted to 9.5 wt% Cr, which implies that austenitization of Crofer 22 H will occur later than in Crofer 22 APU. Furthermore, no austenitization of Crofer 22 H is expected at 900 °C as the alloy is fully ferritic in the entire Cr concentration range. Although Fig. 16**b** predicts austenitization in Crofer 22 H at 950 °C, the austenitization affected zone in Crofer 22 H was experimentally observed only at 1050 °C [11] in the immediate vicinity of the corroded specimen edge, i.e. breakaway oxidation.

4.2. *Beneficial effect of thermal cycling*

The most striking finding in the present study is the effect of thermal history on the chemical life of Crofer 22 APU (Fig. 2 and Fig. 3**b**). Clearly, intermediate cooling, which can also be regarded as thermal cycling had a beneficial effect on the performance of Crofer 22 APU. Despite the significant corrosion attack at the edges (Fig. 4), the middle of the cycled specimen (upper row in Fig. 3**b**) continued to grow external Cr_2O_3 and retained the integrity of the metallic core material for up to 1000 h at 1000 °C albeit the alloy microstructure underwent a profound transformation. At the same time, the isothermal Crofer 22 APU specimens were fully consumed by oxidation after 400 h (Fig. 2 and Fig. 3**b**).

The idea of a beneficial effect of thermal cycling on the long-term performance of a high-temperature alloy during oxidation is highly counterintuitive. Thermal cycling is well-known to accumulate mechanical stresses in the oxide scale [27,28] leading to oxide scale spallation [29,30] especially at sharp edges [31], tensile through-thickness cracking of the oxide scales [32,33] and as result diminished lifetimes [34,35]. To the best of the authors' knowledge, there are no studies in literature questioning this relationship between thermal cycling and protective oxidation or providing any counterevidence.

It is obvious that the classical mechanism "thermal cycling – stresses in the scale – oxide damage – intensified Cr-depletion – breakaway oxidation" is not applicable to the present case for several reasons. First, there is no measurable difference between the weight change of the isothermal and cycled specimens (Fig. 2) and/or oxide scale thickness (Fig. 5) before the onset of breakaway. Thus, there is no detectable Cr_2O_3 spallation or (micro) cracking in the protective oxidation regime. Second, thermal cycling does not affect the weight change of Crofer 22 H (Fig. 2), which substantiates the previous statement and implies that the observed beneficial effect of thermal cycling applies exclusively to Crofer 22 APU (Fig. 3**b**). Third, the main difference between Crofer 22 APU and Crofer 22 H in the present experiment is the formation of a subsurface austenite layer in the former (Fig. 3**b**).

The beneficial effect of thermal cycling on the performance of Crofer 22 APU is thus related to the evolution of the AAZ and the phase

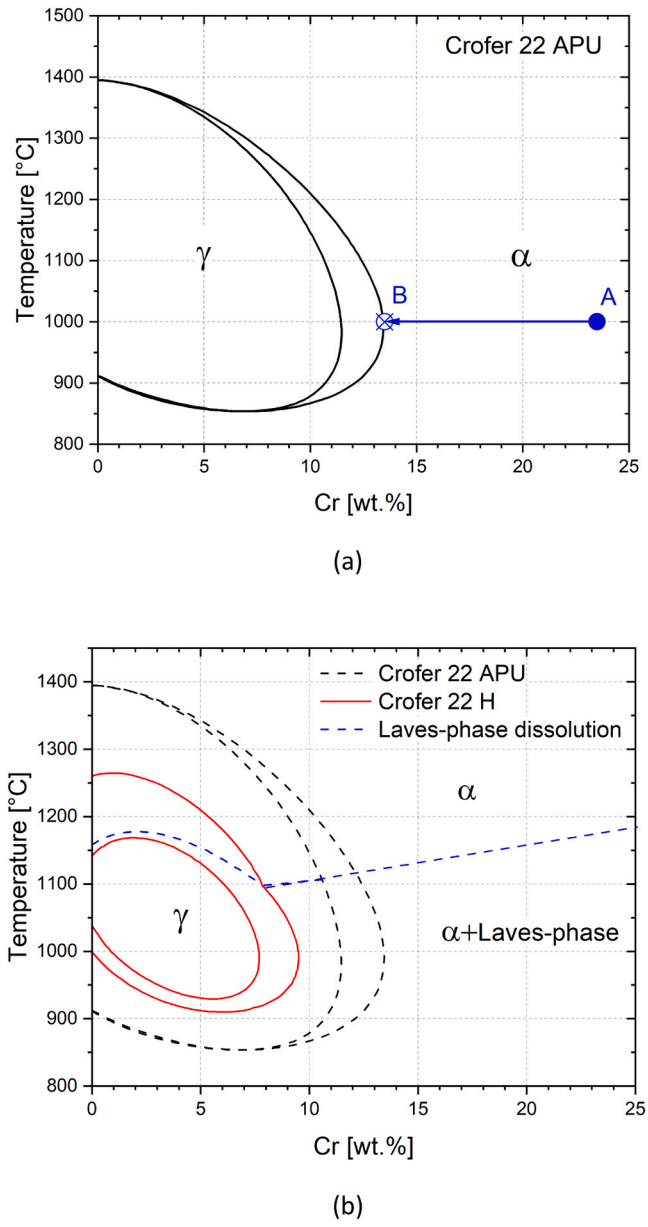

Fig. 16. Austenite loop in (a) Fe-Cr binary phase diagram simulating Crofer 22 APU and in (b) Crofer 22 H calculated with Thermo-Calc using TCFE9 database.

transformations in it [11], but not to the mechanics of the oxide-metal interface and the eventual oxide spalling.

4.3. Thermal cycling and AAZ

The austenitization affected zone (AAZ) in the Crofer 22 APU foils has a characteristic microstructure. The EBSD maps in Fig. 10 as well as TEM images in Fig. 11 revealed a layer of fine-grained, highly misoriented BCC immediately beneath the oxide scale, the average grain size in the AAZ at the oxide-metal interface being 2.5 μm (Fig. 11). Such a dense network of misoriented grain-boundaries (Fig. 10) provides a multitude of short-circuit diffusion paths for Cr to the surface. In contrast to the isothermal exposure, the grains of austenite are expected to nucleate after 225 h according to Fig. 6 and continue to grow. The GB density in this growing austenite layer gradually decreases as the FCC grains grow and coarsen. Cr transport towards the surface is limited mainly to lattice diffusion through the FCC grains. Slower Cr diffusion in FCC compared to BCC and its implication for breakaway oxidation was discussed above (Fig. 9**b**). The Cr concentration profiles in the Crofer 22 APU foil after 400 h at 1000 °C (Fig. 9**b**) are significantly steeper in the isothermal specimen (C_{Cr}^{int} = 11.0 wt%) compared to the cycled specimen (C_{Cr}^{int} = 14.0 wt%). In other words, thermal cycling enhances Cr transport through the AAZ. It needs to be stressed that Cr diffusion in fully ferritic Crofer 22 H (Fig. 9**a**) is not affected by thermal cycling, i.e., the Cr depletion profiles are virtually identical in the isothermal and cycled foils.

Faster Cr diffusion through the AAZ in the cycled Crofer 22 APU specimen is easy to understand. The fine-grained AAZ forms already after the first cooling step (see TEM and compare Fig. (a) with Fig. (b) in Fig. 10). Further heating-cooling cycles additionally refine the microstructure of the AAZ and promote thereby GB diffusion of Cr and its supply to the oxide-metal interface. Another indirect proof of the beneficial effect of thermal cycling via enhanced Cr transport in AAZ is the absence of oxide nodules on the surface of the cycled specimens in contrast to the isothermal ones (Fig. 7).

4.4. Granularity or defects: is one cooling sufficient?

The positive effect of thermal cycling on protective oxidation of Crofer 22 APU is based on the enhanced Cr transport through the fine-grained AAZ due to repetitive recrystallization and grain refinement of this zone during heating-cooling cycles. One question that remains to be answered is what kind of short-circuit diffusion paths dominate in the AAZ: exclusively grain boundaries of the small alloy grains in the AAZs or dislocations and other defects introduced to the microstructure due to recurring phase transformations?

To answer this question, an additional set of specimens was tested in a specific manner. The specimens were cooled only once after 350 h: after the formation of AAZ and before the onset of the isothermal breakaway oxidation. The specimens were re-heated and further exposed isothermally to reach a total exposure duration of 600 and 800 h. Fig. 17 illustrates the effect of one-time cooling. The optical macro images in Fig. 17**a,b** show that the specimens are heavily corroded at the edges. However, the middle of the Crofer 22 APU foil retained extensive areas of protective Cr_2O_3. The SEM BSE images of the cross-sectioned specimen in (Fig. 17**c-i**) demonstrated the initiation of breakaway corrosion at the edges of the foil (Fig. 17**c,d**) and a high degree of integrity of the sound uncorroded metal in the middle of the specimen even after 800 h (Fig. 17**c-h**). This is in stark contrast to the isothermally exposed Crofer 22 APU specimen that is fully corroded after 600 h (Fig. 3). The one-time cooling event is enough for Crofer 22 APU to form the characteristic AAZ layers underneath the Cr_2O_3 scale (Fig. 17**e,g**). The alloy adjacent to the fully corroded edge of the foil (Fig. 17**f,h**) was attacked by internal oxidation and nitridation (Fig. 17**i**, see also Figures S10 and S11 in the **Data supplement**). The characteristic needle-like precipitates containing Cr and N (EDX analysis not shown here) are well-known to appear in post-breakaway alloys [35].

Comparison of the cycled, isothermal and one-time cooled Crofer 22 APU foils is given in Fig. 18. To ensure a reasonable comparison, uncorroded sections in the middle of the cross-sectioned one-time cooled specimens are presented in Fig. 18. Clearly, one cooling is sufficient to prevent or postpone the catastrophic full-scale oxidation observed in the isothermal specimens. At the same time, recurring thermal cycling has a stronger beneficial effect (compare Fig. 4**a** and Fig. 17**d**). The one-time cooling experiment leads to an important conclusion: the main contribution to the enhanced Cr transport through the AAZ is the dense network of the grain boundaries in the fine-grained subsurface AAZ layer which forms already after one single cooling event. Further thermal cycling additionally refines this layer via the nucleation of new fine grains in the subsequent heating-cooling cycles.

EBSD maps in Fig. 19 compare the AAZs in Crofer 22 APU after 800 h at 1000 °C. The sample in Fig. 19**a** experienced thermal cycling every 100 h while the sample in Fig. 19**b** was subject to a one-time cooling

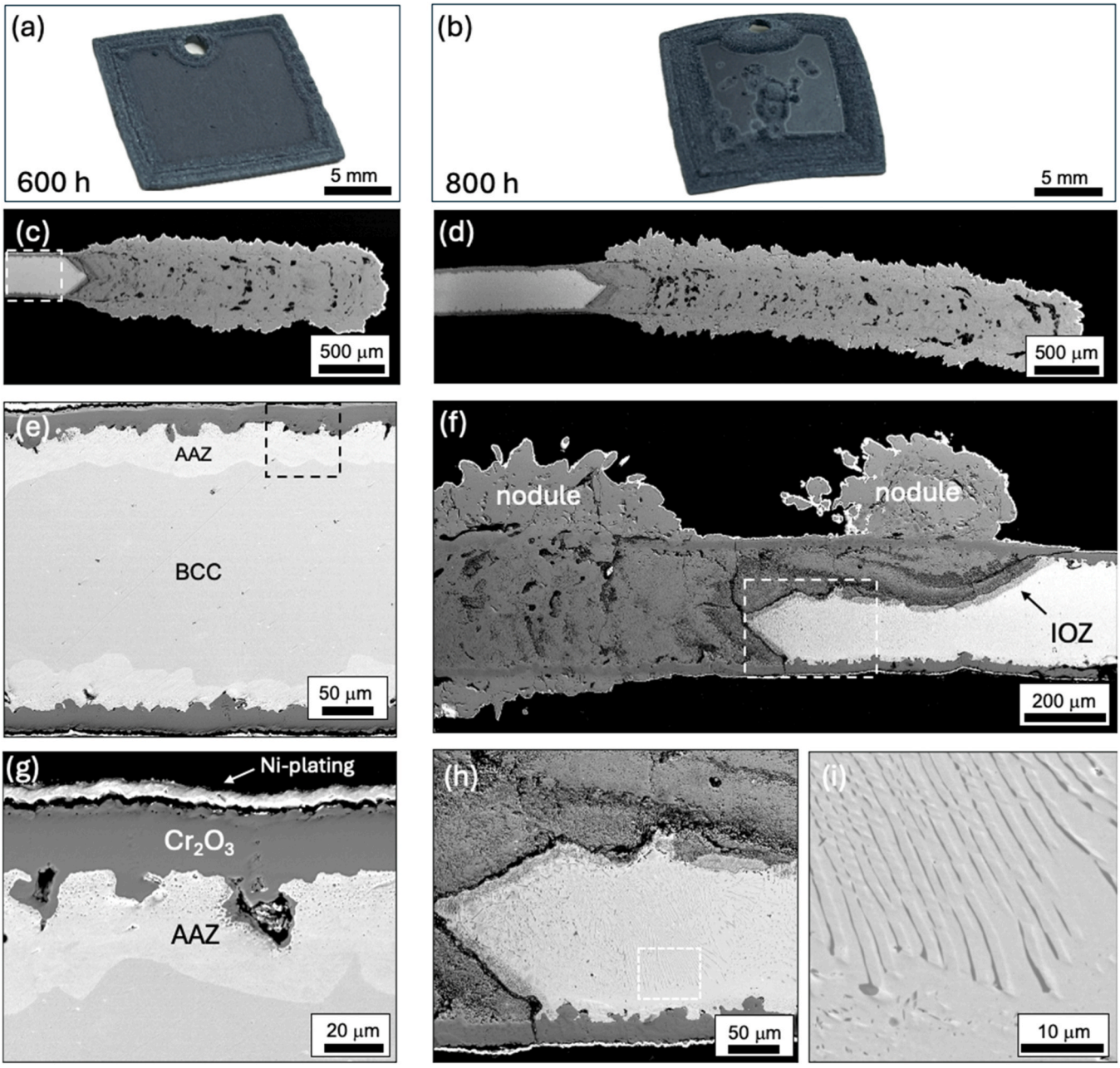

Fig. 17. Effect of one cooling on isothermal air oxidation of Crofer 22 APU at 1000 °C. The 0.3 mm thick foil specimens were isothermally exposed for 350 h at 1000 °C, cooled to room temperature and further isothermally exposed for a total duration of 600 h (Figs. a,c,e,g) and 800 h (Figs. b,d,f,h). Optical macro-images in (a,b) demonstrate the overall corrosion damage. SEM BSE images in (c-h) illustrate cross-sectioned specimens. The frame in fig. (f) delineates fig. (h) while the frame in fig (h) delineates fig. (i).

event after 350 h (presented in Fig. 17**c-h)**. The EBSD maps show a finer grain structure in the AAZ of the specimen that has been exposed under cyclic conditions. The grain size histogram in Fig. 19**c** reveals a peak of the average equivalent diameter at 15 µm for this sample. The grain size distribution in the AAZ in the one-time cooled specimen (Fig. 19**d**) shows the AAZ contains two populations of grains, i.e., the smaller ones (average equivalent diameter of 15 µm) closer to the oxide-metal interface (Fig. 19**b**) and larger grains (average equivalent diameter of 39 µm) at the bottom of the AAZ. Clearly, multiple thermal cycles resulted in a refinement of these larger grains closer to the ferritic alloy matrix and thus additionally promoted faster Cr diffusion through the AAZ.

5. Conclusions

This study presents two major experimental findings with respect to breakaway oxidation of ferritic stainless steels exposed to oxidizing environments above 900 °C.

First, the formation of austenite during oxidation of a ferritic stainless steel, Crofer 22 APU in the present case, was experimentally evidenced by means of in-situ high-temperature XRD of the pulverized Crofer 22 APU. Oxidation of steel particles 15–45 µm in diameter at 900 and 1000 °C rapidly depleted them of Cr and induced the α-to-γ transformation which was directly detected in the in-situ diffractograms. The previous conclusions about the austenitization-driven nature of this breakaway oxidation mechanism were based on the circumstantial evidence such as a beneficial effect of the ferrite-stabilizing alloying

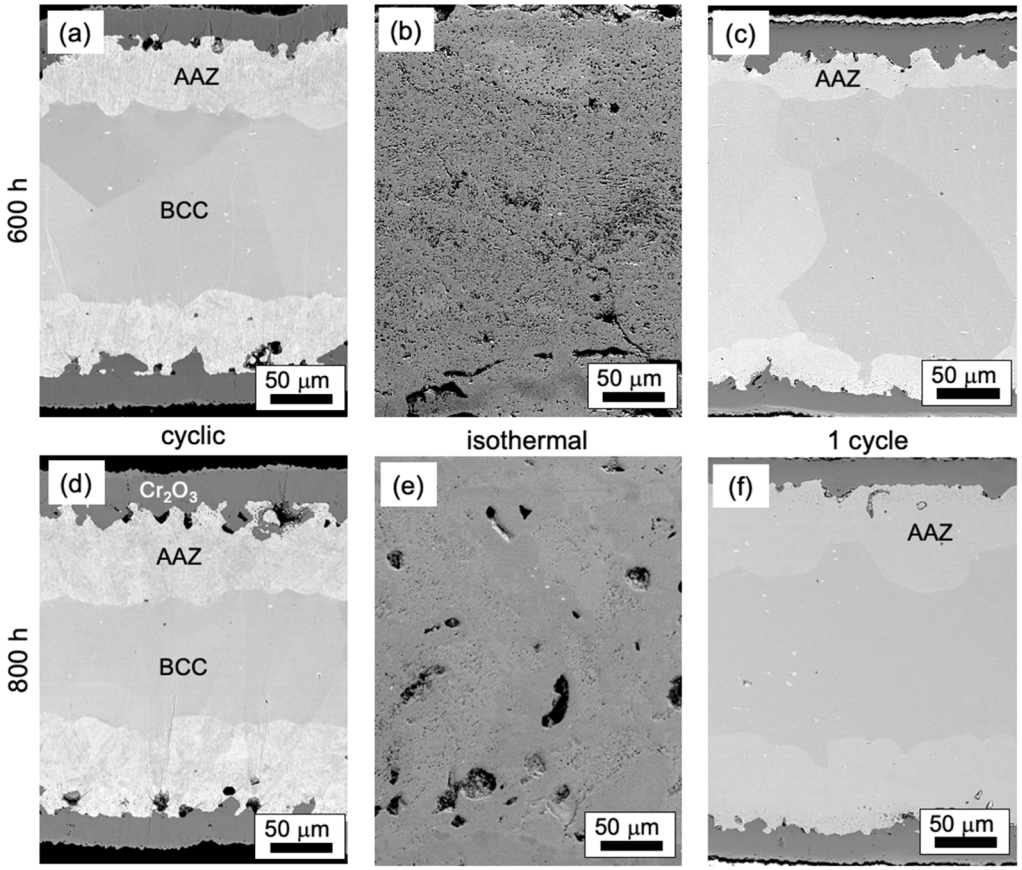

Fig. 18. SEM BSE images of cross-sectioned Crofer 22 APU specimens after (a-c) 600 and (d-f) 800 h of air oxidation at 1000 °C: comparison of (a,d) cyclic, (b,e) isothermal (c,f) and one-cooling exposures. Areas of sound uncorroded metal are displayed in (c,f).

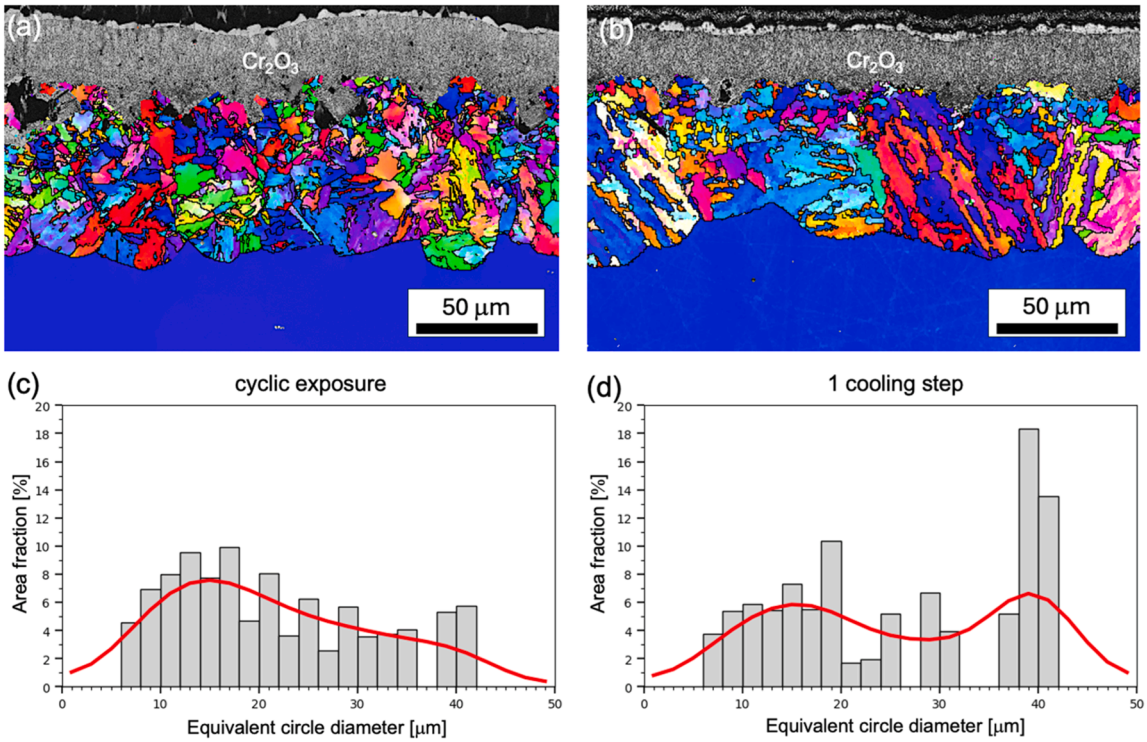

Fig. 19. EBSD maps (a,b) and grain size distribution (c,d) within AAZ in foils of Crofer 22 APU after 800 h air exposure at 1000 °C: (a,c) the specimen cooled every 100 h, (b,d) the specimen intermediately cooled only once after 350 h.

additions or post-exposure analyses of the austenitization affected zones (AAZ).

Second, thermal cycling was found beneficial for the Crofer 22 APU exposed in air for up to 1000 h at 1000 °C while the isothermally exposed specimens of Crofer 22 APU suffered from catastrophic through-thickness (0.3 mm) oxidation already after 400 h. At the same time, no effect of thermal history was detected for Crofer 22 H. The abnormal behavior of Crofer 22 APU is related to the formation of the AAZ at the oxide-metal interface. The austenitic layer impeded Cr diffusion to the alloy surface thereby facilitating breakaway oxidation. The heating-cooling cycles result in the transformation of the newly formed austenite back into ferrite upon cooling. The re-formed ferrite in the AAZ is highly fine-grained and provides multiple short-circuit diffusion paths for Cr transport through the AAZ resulting in a more protective oxidation behavior of the alloy during thermal cycling compared to isothermal exposure.

CRediT authorship contribution statement

Anton Chyrkin: Conceptualization, Investigation, Writing - original draft, Writing - review & editing, Funding acquisition, Project administration. **D. Naumenko:** Writing - review & editing, Project administration. **M. Ziegner:** Investigation. **E. Wessle:** Investigation. **Mohammad Sattari:** Investigation. **Jan Froitzheim:** Writing - review & editing, Funding acquisition, Project administration.

Declaration of Competing Interest

The authors declare that they have no known competing financial interests or personal relationships that could have appeared to influence the work reported in this paper.

Acknowledgements

This work was funded by the Swedish Foundation for Strategic Research SSF under Grant No. UKR22–0047. Furthermore, the authors acknowledge support by the MoreH2 project, a part of the Nordic Grand Solutions Programme funded by Nordic Energy Research. Chalmers Materials Analysis Laboratory (CMAL) is acknowledged for the access to the analytical facilities. Dr. V. Ssenteza from Chalmers University of Technology is acknowledged for assisting with the EBSD analysis. Colleagues of Forschungszentrum Jülich GmbH (IMD-1) are acknowledged for performing the TG-experiments (Mr. H. Cosler) and metallographic preparation (Mr. J. Bartsch), respectively. All persons who have made substantial contributions to the work reported in the manuscript (e.g., technical help, writing and editing assistance, general support), but who do not meet the criteria for authorship, are named in the Acknowledgements and have given us their written permission to be named. If we have not included an Acknowledgements, then that indicates that we have not received substantial contributions from non-authors.

Appendix A. Supporting information

Supplementary data associated with this article can be found in the online version at doi:10.1016/j.corsci.2026.113779.

Data Availability

Data will be made available on request.

References

[1] P. Spätig, J.C. Chen, G.Robert Odette, Ferritic and tempered martensitic steels, Struct. Alloy. Nucl. Energy Appl. (2019) 485–527, https://doi.org/10.1016/B978-0-12-397046-6.00011-3.
[2] L. Faivre, P.O. Santacreu, A. Acher, A new ferritic stainless steel with improved thermo-mechanical fatigue resistance for exhaust parts, Mater. High. Temp. 30 (2013) 36–42, https://doi.org/10.3184/096034013X13637176323444.
[3] A. Shibli, Boiler steels, damage mechanisms, inspection and life assessment, Power Plant Life Manag. Perform. Improv. (2011) 272–303, https://doi.org/10.1533/9780857093806.2.272.
[4] W.J. Quadakkers, J. Piron-Abellan, V. Shemet, L. Singheiser, Metallic interconnectors for solid oxide fuel cells–a review, Mater. High. Temp. 20 (2003) 115–127, https://doi.org/10.3184/096034003782749071.
[5] K. Chen, S.P. Jiang, Review—Materials degradation of solid oxide electrolysis cells, J. Electrochem. Soc. 163 (2016) F3070–F3083, https://doi.org/10.1149/2.0101611jes.
[6] A. Nechache, S. Hody, Alternative and innovative solid oxide electrolysis cell materials: a short review, Renew. Sustain. Energy Rev. 149 (2021) 111322, https://doi.org/10.1016/J.RSER.2021.111322.
[7] W.J. Quadakkers, M.J. Bennett, Oxidation induced lifetime limits of thin walled, iron based, alumina forming, oxide dispersion strengthened alloy components, Mater. Sci. Technol. 10 (1994) 126–131, https://doi.org/10.1179/MST.1994.10.2.126.
[8] P. Huczkowski, N. Christiansen, V. Shemet, J. Piron-Abellan, L. Singheiser, W. J. Quadakkers, Oxidation limited life times of chromia forming ferritic steels, Mater. Corros. 55 (2004) 825–830, https://doi.org/10.1002/MACO.200303798.
[9] D.P. Whittle, The oxidation of finite samples of heat-resistant alloys, Corros. Sci. 12 (1972) 869–872, https://doi.org/10.1016/S0010-938X(72)80016-7.
[10] H.C. Cowen, S.J. Webster, Chromium depletion during oxidation of stainless steel foils, Proceedings of the British Nuclear Energy Society, International Conference at Reading University, 23-24 September 1974. (1974) 349–358.
[11] A. Chyrkin, J. Froitzheim, Premature breakaway oxidation of ferritic stainless steels triggered by austenitization, Corros. Sci. 256 (2025) 113260, https://doi.org/10.1016/J.CORSCI.2025.113260.
[12] D.P. Whittle, G.C. Wood, D.J. Evans, D.B. Scully, Concentration profiles in the underlying alloy during the oxidation of iron-chromium alloys, Acta Metall. 15 (1967) 1747–1755, https://doi.org/10.1016/0001-6160(67)90066-1.
[13] D.J. Young, J. Zurek, L. Singheiser, W.J. Quadakkers, Temperature dependence of oxide scale formation on high-Cr ferritic steels in Ar-H2-H2O, Corros. Sci. 53 (2011) 2131–2141, https://doi.org/10.1016/j.corsci.2011.02.031.
[14] J. Zurek, G.H. Meier, E. Wessel, L. Singheiser, W.J. Quadakkers, Temperature and gas composition dependence of internal oxidation kinetics of an Fe-10%Cr alloy in water vapour containing environments, Mater. Corros. 62 (2011) 504–513, https://doi.org/10.1002/maco.201005865.
[15] A. Chyrkin, J. Froitzheim, J. Zurek, D. Naumenko, Austenitization triggering breakaway oxidation of FeCr-base alloys at 900 °C, Corros. Sci. 244 (2025) 112605, https://doi.org/10.1016/J.CORSCI.2024.112605.
[16] A. Chyrkin, W.J. Quadakkers, Effect of α-to-γ transformation on internal oxidation in FeCr-base alloys in dry and wet gases, J. Alloy. Compd. 1045 (2025) 184722, https://doi.org/10.1016/J.JALLCOM.2025.184722.
[17] M. Klinger, A. Jäger, Crystallographic Tool Box (CrysTBox): automated tools for transmission electron microscopists and crystallographers, J. Appl. Crystallogr 48 (2015) 2012, https://doi.org/10.1107/S1600576715017252.
[18] N. Mortazavi, M. Esmaily, M. Halvarsson, The capability of Transmission Kikuchi Diffraction technique for characterizing nano-grained oxide scales formed on a FeCrAl stainless steel, Mater. Lett. 147 (2015) 42–45, https://doi.org/10.1016/J.MATLET.2015.02.008.
[19] P.I. Williams, R.G. Faulkner, Chemical volume diffusion coefficients for stainless steel corrosion studies, J. Mater. Sci. 22 (1987) 3537–3542, https://doi.org/10.1007/BF01161455/METRICS.
[20] J. Froitzheim, G.H. Meier, L. Niewolak, P. Ennis, H. Hattendorf, L. Singheiser, W. J. Quadakkers, Development of high strength ferritic steel for interconnect application in SOFCs, J. Power Sources 178 (2008) 163–173, https://doi.org/10.1016/j.jpowsour.2007.12.028.
[21] B. Kuhn, C.A. Jimenez, L. Niewolak, T. Hüttel, T. Beck, H. Hattendorf, L. Singheiser, W.J. Quadakkers, Effect of Laves phase strengthening on the mechanical properties of high Cr ferritic steels for solid oxide fuel cell interconnect application, Materials Science Engineering A 528 (2011) 5888–5899, https://doi.org/10.1016/j.msea.2011.03.112.
[22] C. Asensio-Jimenez, L. Niewolak, H. Hattendorf, B. Kuhn, P. Huczkowski, L. Singheiser, W.J. Quadakkers, Effect of specimen thickness on the oxidation rate of high chromium ferritic steels: The significance of intrinsic alloy creep strength, Oxid. Met. 79 (2013) 15–28, https://doi.org/10.1007/s11085-012-9323-5.
[23] O.K. von Goldbeck, Iron—Chromium Fe—Cr, IRON Bin. Phase Diagr. (1982) 31–34, https://doi.org/10.1007/978-3-662-08024-5_17.
[24] Thermo-Calc, TCFE6 - TCS Steels/Fe-Alloys Database, Version 6.2, (2013).
[25] W.J. Quadakkers, D. Naumenko, S. Weinbruch, I. Gurrappa, Factors governing breakaway oxidation of FeCrAl-based alloys, Mater. Corros. 51 (2002) 224–235, https://doi.org/10.1002/(SICI)1521-4176(200004)51:4.
[26] W. Gordon, A. Van Bennekom, Review of stabilisation of ferritic stainless steels, Mater. Sci. Technol. 12 (1996) 126–131, https://doi.org/10.1179/MST.1996.12.2.126.
[27] H.E. Evans, Stress effects in high temperature oxidation of metals, Int. Mater. Rev. 40 (1995) 1–40, https://doi.org/10.1179/IMR.1995.40.1.1.
[28] D.P. Whittle, Spalling of protective oxide scales, Oxid. Met. 4 (1972) 171–179, https://doi.org/10.1007/BF00613091/METRICS.
[29] L. Niewolak, M. Malessa, S.Y. Coleman, W.J. Quadakkers, M. Schütze, Influence of cycling parameter variation on thermal cyclic oxidation testing of high temperature materials (COTEST), Mater. Corros. 57 (2006) 31–42, https://doi.org/10.1002/MACO.200503892.

[30] A. Galerie, F. Toscan, M. Dupeux, J. Mougin, G. Lucazeau, C. Valot, A.-M. Huntz, L. Antoni, Stress and adhesion of chromia-rich scales on ferritic stainless steels in relation with spallation, Mater. Res. 7 (2004) 81–88, https://doi.org/10.1590/S1516-14392004000100012.
[31] H.E. Evans, A.T. Donaldson, T.C. Gilmour, Mechanisms of breakaway oxidation and application to a chromia-forming steel, Oxid. Met. 52 (1999) 379–402, https://doi.org/10.1023/A:1018855914737/METRICS.
[32] A. Chyrkin, N. Mortazavi, M. Halvarsson, D. Grüner, W.J. Quadakkers, Effect of thermal cycling on protective properties of alumina scale grown on thin Haynes 214 foil, Corros. Sci. 98 (2015), https://doi.org/10.1016/j.corsci.2015.06.020.
[33] S. Osgerby, K. Berriche-Bouhanek, H.E. Evans, Tensile cracking of a chromia layer on a stainless steel during thermal cycling with hold periods, Mater. Sci. Eng. A 412 (2005) 182–190, https://doi.org/10.1016/j.msea.2005.08.193.
[34] J.L. Smialek, A deterministic interfacial cyclic oxidation spalling model, Acta Mater. 51 (2003) 469–483, https://doi.org/10.1016/S1359-6454(02)00430-5.
[35] R. Pillai, A. Chyrkin, W.J. Quadakkers, Modeling in high temperature corrosion: a review and outlook, Oxid. Met. 96 (2021), https://doi.org/10.1007/s11085-021-10033-y.